Capillarity

Vol. 18, No. 1, p. 27-40, 2026

Original article

Density-driven convection in layered and stochastically heterogeneous formations: Implications for CO_2 geological sequestratione

Yaohui Wang[1,2], Fugang Wang[1,2], Junwen Wang[1,2], Donghui Wang[3], Qingcheng He[4], Hui Cheng[1,2]*

[1]*Key Laboratory of Groundwater Resources and Environment, Ministry of Education, Jilin University, Changchun 130012, P. R. China*
[2]*Jilin Provincial Key Laboratory of Water Resources and Water Environment, Changchun 130012, P. R. China*
[3]*Chengdu Center, China Geological Survey, Chengdu 610081, P. R. China*
[4]*Deep Earth Exploration Center, Chinese Academy of Geological Sciences, Beijing 100037, P. R. China*

Keywords:
Geological carbon sequestration
density-driven convection
solubility trapping
stratigraphic heterogeneity

Cited as:
Wang, Y., Wang, F., Wang, J., Wang, D., He, D., Cheng, H. Density-driven convection in layered and stochastically heterogeneous formations: Implications for CO_2 geological sequestratione. Capillarity, 2026, 18(1): 27-40.
https://doi.org/10.46690/capi.2026.01.03

Abstract:
Geological carbon sequestration relies on the efficient conversion of injected supercritical CO_2 into dissolved CO_2, a process accelerated by density-driven convection. Yet, most assessments still consider the subsurface as homogeneous, offering limited guidance for the layered and heterogeneous architectures typical of sedimentary basins. Building on this shortcoming, this work examines how stratigraphic structure – such as homogeneous, randomly layered, stochastic, positive rhythmic, reverse rhythmic, coarse-first, and fine-first formations – governs the onset and efficiency of convective dissolution. Using a two-dimensional model, this work tracks the dissolved-to-total CO_2 mass fraction and relate system-scale kinetics to plume morphology. The findings reveal that stratigraphy exerts first-order control on both the timing and mode of CO_2 transformation. Architectures with high-permeability pathways near the top, or those with strong small-scale heterogeneity, trigger early convection, promote vertically continuous fingering, and accelerate dissolution relative to a homogeneous benchmark. Randomly layered formations that divert flow produce moderate slowdowns. In contrast, low-permeability caps suppress vertical exchange, favor lateral spreading, and substantially delay conversion; coarse-first formations exhibit early lateral channeling that retards late-time mixing. Overall, the distribution of permeability in the upper reservoir and the scale of heterogeneity jointly control convective onset and dissolution efficiency, providing actionable guidance for formation screening, well placement, and monitoring horizons in geological carbon sequestration projects.

1. Introduction

Anthropogenic carbon dioxide (CO_2) emissions are dominant in driving climate change and its associated impacts on ecosystems, human health, and economic stability; therefore, its mitigation is an urgent global task (Li et al., 2024). Geological carbon sequestration (GCS) is widely recognized as one of the most promising technologies for achieving deep decarbonization while maintaining energy security (Wang et al., 2024; Faramarzi et al., 2025). Through injection into deep geological formations, such as saline aquifers, depleted oil and gas reservoirs, and unmineable coal seams, large amounts of CO_2 can be isolated from the atmosphere for millennia

Yandy Scientific Press

*Corresponding author.
E-mail address: yaohuiw24@mails.jlu.edu.cn (Y. Wang); wangfugang@jlu.edu.cn (F. Wang); jwwang25@mails.jlu.edu.cn (J. Wang); dong_hui_wang@163.com (D. Wang); qingcheng_he@126.com (Q. He); chenghui22@mails.jlu.edu.cn (H. Cheng).

Received November 14, 2025; revised December 16, 2025; accepted January 1, 2026; available online January 3, 2026.

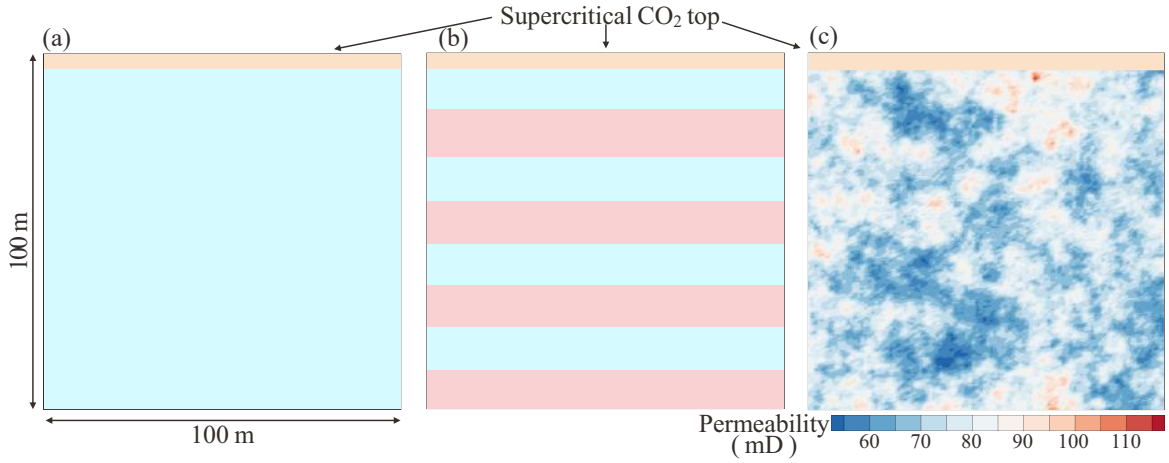

Fig. 1. Schematic diagrams of conceptual geological models for simulating CO_2 density-driven convection. (a) Homogeneous, (b) heterogeneous (layered) and (c) heterogeneous (normal distribution).

(Bachu, 2008; Xue et al., 2025). Among these options, deep saline aquifers are regarded as having the largest sequestration capacity worldwide, making them the focus of both pilot and commercial-scale projects (Michael et al., 2010; Szulczewski et al., 2012; Umirova et al., 2025).

When injected underground, CO_2 is typically in a supercritical state, characterized by high mobility and buoyancy compared with the resident brine (Guo et al., 2021; Wang et al., 2021; Awag et al., 2024b). Subsequent CO_2 migration is governed by a combination of multiphase flow processes, capillary trapping, dissolution trapping, and mineral trapping (Juanes et al., 2006; Benson and Cole, 2008; Awag et al., 2024a). Among these, dissolution trapping, whereby CO_2 dissolves into brine and its density increases, gives rise to convective density-driven flows, also termed as "convective dissolution" or "density-driven convection" (Riaz et al., 2006; Hu et al., 2023; Liu et al., 2024). Such flows enhance mixing and significantly accelerate the long-term stabilization of CO_2 by reducing the amount of mobile free-phase CO_2 (Brouzet et al., 2022; Mahyapour et al., 2022; Fruton et al., 2023). Conversely, the development and morphology of convective plumes can also alter CO_2 distribution in aquifers, thereby influencing sequestration efficiency and security (Neufeld et al., 2010; MacMinn and Juanes, 2013; Slim, 2014).

The onset and dynamics of density-driven convection are strongly controlled by geological heterogeneity (Amarasinghe et al., 2021; Luther et al., 2022; Soboleva, 2023). Most GCS projects are located in sedimentary basins where reservoir formations are rarely homogeneous (Benson and Cole, 2008; Wang et al., 2022, 2025; Zhang et al., 2024). In fact, they exhibit a wide variety of stratigraphic architectures, such as coarsening-upward sequences (normal rhythmic layering), fining-upward sequences (inverse rhythmic layering), alternations of high- and low-permeability strata, or stochastic heterogeneity associated with depositional environments (Sayers et al., 2011; De Paoli et al., 2016; Jing et al., 2025). Research has demonstrated that heterogeneity can enhance or suppress convective mixing, depending on the connectivity and anisotropy of the porous structure (Pau et al., 2010; Emami-Meybodi et al., 2015; Li and Benson, 2015). For instance, permeability layering can redirect CO_2 plumes laterally, while small-scale heterogeneity may inhibit vertical convective fingers (Hidalgo and Carrera, 2009; Li et al., 2025).

Despite advances in theoretical, experimental and numerical studies of density-driven convection, several important gaps remain (Amarasinghe et al., 2021; Mahyapour et al., 2022; Shahriar and Khanal, 2023). The majority of existing works assume homogeneous or weakly heterogeneous formations, therefore they fail to capture the true complexity of stratified and stochastic reservoir architectures (Hesse et al., 2008; Hidalgo et al., 2012; Slim, 2014). Moreover, systematic analyses comparing different stratigraphic types, such as rhythmic layering versus stochastic heterogeneity, are scarce (Sayakov et al., 2025). As a result, current predictions of convective dissolution dynamics may oversimplify the effects of geological heterogeneity, limiting their applicability to real-world reservoirs.

To address the aforementioned gaps, the present study designs a suite of conceptual stratigraphic models, including rhythmic, alternating and stochastic heterogeneity. By conducting high-resolution numerical simulations, this work systematically investigates the impact of stratigraphic architecture on the development of density-driven convective flows during CO_2 geological sequestration. The findings contribute to a more robust understanding of how heterogeneity influences convective dissolution, with implications for improving the assessment of sequestration security and the long-term performance of CO_2 sequestration projects.

2. Materials and Methods

2.1 Conceptual model

To reproduce CO_2 density-driven convection, the present study introduces a supercritical CO_2-saturated layer at the top of the formation, thereby simulating the post-injection buoyant accumulation of CO_2. Three types of geological models were constructed based on three respective processes: Homogeneous formation (Fig. 1(a)), stratified heterogeneous formation (Fig.

Table 1. Permeability distributions for different formation models (mD).

Layer	Positive rhythm	Reverse rhythm	Coarse-first	Fine-first	Randomly layered
0	75.0	75.0	75.0	75.0	75.0
1	10.5	139.8	145.0	5.0	62.1
2	16.2	133.8	5.0	145.0	95.4
3	21.8	128.8	145.0	5.0	85.1
4	27.4	122.8	5.0	145.0	56.7
5	33.0	116.8	145.0	5.0	62.8
6	38.7	111.8	5.0	145.0	51.6
7	44.3	105.8	145.0	5.0	83.6
8	49.9	100.3	5.0	145.0	51.5
9	55.5	94.7	145.0	5.0	69.2
10	61.2	89.1	5.0	145.0	68.4
11	66.8	83.4	145.0	5.0	62.7
12	72.4	77.8	5.0	145.0	73.2
13	78.0	72.2	145.0	5.0	62.9
14	83.7	66.6	5.0	145.0	88.4
15	89.3	60.9	145.0	5.0	103.3
16	94.9	55.3	5.0	145.0	69.1
17	100.4	49.7	145.0	5.0	56.5
18	106.4	44.1	5.0	145.0	105.3
19	111.4	38.4	145.0	5.0	101.0
20	117.4	32.8	5.0	145.0	72.0
21	123.4	27.2	145.0	5.0	57.4
22	128.4	21.6	5.0	145.0	94.7
23	134.4	15.9	145.0	5.0	73.7
24	140.4	10.3	5.0	145.0	94.3

1(b)), and stochastically heterogeneous formation following normal distribution (Fig. 1(c)). The differences between these models lie in the spatial variability of porosity and permeability as follows:

1) In the homogeneous formation model, porosity and permeability are uniform throughout the entire formation.
2) In the stratified heterogeneous formation model, porosity and permeability are discretized into multiple horizontal layers. Depending on the sequential arrangement of porosity-permeability values, the stratified model is further classified into:
   a) A positive rhythm sequence, in which porosity and permeability gradually increase.
   b) A reverse rhythm sequence, in which porosity and permeability gradually decrease.
   c) An alternating sequence, in which high and low porosity-permeability values appear in alternation. Within this type, two subtypes are distinguished according to the properties of the first layer in contact with supercritical CO_2: A coarse-first sequence (initially high porosity-permeability) and a fine-first sequence (initially low porosity-permeability).
   d) A randomly layered sequence, in which the porosity and permeability of each layer are randomly distributed but still follow a stratified structure.
3) In the stochastic model, porosity and permeability are randomly distributed but follow an overall normal distribution.

The permeability parameters of the different formation types are summarized in Table 1. The formation model was divided into 25 layers of equal thickness, with each layer being 4 m. At the top of the formation, Layer 0 was initially saturated with supercritical CO_2, and its permeability was uniformly set to 75 mD. Layers 1-24 were initially saturated with brine, and their permeabilities varied depending on the specific geological model. The average permeability of all models was 75 mD. Porosity and permeability were treated as covariant properties. In this study, the permeability of each layer in the homogeneous model was 75 mD. Besides, the stochastic permeability field was generated from a normal distribution (mean = 75 mD, standard deviation = 13.82 mD), with spatial dependence introduced through an exponential covariance model and a horizontal correlation.

2.2 Mathematical model

The migration and transport of CO_2 in saturated porous media are governed by a mathematical framework (Eqs. (1)-(3)) derived from the conservation of mass, energy and momentum (Pruess, 2004; Ajayi and Gupta, 2019). The general form of the mass conservation equation can be expressed as:

$$\frac{\partial}{\partial t}\left[\phi\left(S_l\rho_l X_{wl}+S_g\rho_g X_{wg}\right)\right]=-\nabla\left(X_{wl}\rho_l\boldsymbol{u}_l+X_{wg}\rho_g\boldsymbol{u}_g\right)+q_w \tag{1}$$

$$\frac{\partial}{\partial t}\left[\phi\left(S_l\rho_l X_{cl}+S_g\rho_g X_{cg}\right)\right]=-\nabla\left(X_{cl}\rho_l\boldsymbol{u}_l+X_{cg}\rho_g\boldsymbol{u}_g\right)+q_c \tag{2}$$

$$\begin{aligned}&\frac{\partial}{\partial t}\left[\phi\left(S_l\rho_l U_l+S_g\rho_g U_g\right)+(1-\phi)\rho_s U_s\right]=\\&-\nabla\left(\sum_{i=g,l}H_i\rho_i\boldsymbol{u}_i-h\nabla T\right)+q_h\end{aligned} \tag{3}$$

where the subscripts g, l and s represent the gas, liquid and solid phases, and w and c denote brine and CO_2, respectively; ϕ represents the porosity; S denotes the saturation; ρ denotes the density, kg/m^3; X denotes the mass fraction; q is the source/sink term (kg/(m^3·s)); U denotes the internal energy, J/kg; H denotes the heat, J; h denotes heat conductivity, W/(m·K); T represents the temperature, °C; q_h denotes the source/sink terms of energy, J/(m^3·s); $\boldsymbol{u}$ denotes the Darcy velocity vector, m/s; t is the time, s.

Given that CO_2 migrates at a relatively slow rate during geological sequestration, its movement can be described by Darcy's law. When inertial and macroscopic viscous effects are negligible, the momentum balance for each phase under gravitational influence is represented by the multiphase form of Darcy's law (Pruess, 2004):

Table 2. Main parameters of the model.

Parameters	Values
Total formation thickness (m)	100
Salinity (-)	0.03
Heat conductivity (W/(m·°C))	2.51
Specific heat capacity (J/(kg·°C))	920
Rock density (kg/m^3)	2,600
Compressibility (Pa^{-1})	4.5×10^{-10}
Residual liquid saturation (-)	0.15
Residual gas saturation (-)	0.05
λ (van Genuchten model) (-)	0.457

$$\boldsymbol{u}_i = -k\left(\frac{k_{ri}}{\mu_i}\right)(\nabla P_i - \rho_i \boldsymbol{g}) \quad i = g, l \tag{4}$$

where k represents the permeability, m^2; k_r denotes the relative permeability; μ denotes the viscosity, kg/(m·s); P denotes the pressure, Pa; and $\boldsymbol{g}$ is the gravitational acceleration, m/s^2.

The relative permeabilities of the gas and liquid phases are characterized by the Corey model (Eqs. (5) and (6)) and the van Genuchten model (Eqs. (7) and (8)), whereas capillary pressure is represented using the van Genuchten formulation (Eqs. (8) and (9)) (Corey, 1954; van Genuchten, 1980):

$$k_{rg} = (1-\hat{S})^2(1-\hat{S}^2) \tag{5}$$

$$\hat{S} = \frac{S_l - S_{lr}}{1 - S_{lr} - S_{gr}} \tag{6}$$

$$k_{rl} = (S^*)^{1/2}\left\{1 - \left[1 - (S^*)^{1/\lambda}\right]^{\lambda}\right\}^2 \tag{7}$$

$$S^* = \frac{S_l - S_{lr}}{1 - S_{lr}} \tag{8}$$

$$P_c = -P_s\left[(S^*)^{-1/\lambda} - 1\right]^{1-\lambda} \tag{9}$$

where S_{lr} represents the residual liquid phase saturation; S_{gr} represents the residual gas saturation; λ represents the model exponent; P_c denotes the capillary pressure, Pa; and P_s is the strength coefficient, Pa.

2.3 Numerical model

Building on the above conceptual models and mathematical formulations, a numerical simulation was conducted with TOUGH2-ECO2N. TOUGH2 is a general-purpose simulator for multiphase fluid flow and hydrothermal processes (Pruess, 2004), while ECO2N (version 2.0) is its EOS module specifically developed to model CO_2 sequestration in saline aquifers under typical reservoir conditions (10 °C ≤ T ≤ 110 °C; P ≤ 600 bar) (Pruess and Spycher, 2007).

2.3.1 Mesh generation

Grid discretization was carried out using Meshmaker, a software developed specifically for gridding in the TOUGH code series. In this study, the model was discretized into a two-dimensional grid. Along the horizontal direction (X-axis), the domain was divided into 100 cells with a spacing of 1 m, while in the vertical direction (Z-axis), it was divided into 200 cells with a spacing of 0.5 m. In total, the model comprised 20,000 grid cells.

2.3.2 Initial and boundary conditions

When defining the temperature and pressure boundary conditions, this study used the formation pressure and temperature data of the Shijianfeng Formation from the Shenhua GCS demonstration project in the Ordos Basin, China, as a reference to better simulate realistic engineering conditions. According to published data (Jing et al., 2021), the initial formation pressure was calculated using the hydrostatic pressure equilibrium method (Eq. (10)). The initial model temperature was determined for each layer using the depth-temperature relationship measured prior to injection (Eq. (11)). The initial CO_2 saturation S_g in the original formation was 0 and the liquid saturation S_l was 1. The actual water sample test results indicated an initial salinity of 0.03:

$$P(z,t) = \rho_w g z + 171 \times 10^5 \tag{10}$$

$$T(z,t) = 0.0268z + 56 \tag{11}$$

where P represents the formation pressure, Pa; z denotes the depth, m; and ρ_w is the water density, kg/m^3.

To simulate the transformation of supercritical CO_2 accumulated at the top of the reservoir into the dissolved phase and the subsequent development of density-driven convection, all four boundaries of the two-dimensional model (top, bottom and lateral) were specified as Neumann zero-flux boundaries (second-type boundaries).

In this study, the supercritical CO_2 source was modeled as a mobile free-phase CO_2 region with a finite initial volume. The free CO_2 accumulates beneath the top boundary and gradually dissolves into the brine following local phase-equilibrium conditions. As dissolution progresses, the free-phase volume decreases continuously until the supercritical CO_2 is fully depleted. After depletion, no additional CO_2 enters the system, and the subsequent evolution is governed solely by the density-driven convection of the dissolved phase.

2.3.3 Main parameters

To better reflect the realistic engineering conditions, the petrophysical parameters of the Shiqianfeng Formation from the Shenhua GCS demonstration project in the Ordos Basin, China, were adopted as input parameters for this study. The detailed data are provided in Table 2.

2.3.4 Simulation scheme of the model

From the stratigraphic models established in Section 2.1, three categories of simulation schemes were designed in this study: Case 1, homogeneous formation; Case 2-1, positive rhythmic formation; Case 2-2, reverse rhythmic formation; Case 2-3, coarse-first formation; Case 2-4, fine-first formation; Case 2-5, randomly layered formation; and Case 3, stochastic formation. The corresponding stratigraphic models for each case are presented in Table 1.

3. Results and discussion

3.1 Onset time of density-driven convection

The onset time of density-driven convection differed markedly among the various stratigraphic configurations. In the homogeneous formation, convection initiated after 35.22 years, indicating that in the absence of heterogeneity, the gravitational instability develops relatively quickly once sufficient CO_2 dissolves into the brine to produce a density contrast. In contrast, the positive rhythmic formation exhibited a substantially delayed onset of 338.91 years, and the fine-first formation showed the longest onset time of 885.34 years. This pronounced delay was likely attributable to the presence of low-permeability layers at the top of the reservoir, which impeded vertical mass transfer and effectively suppressed the initial growth of convective fingers.

By comparison, the reverse rhythmic (23.56 years), coarse-first (18.85 years), and randomly layered (43.36 years) formations showed intermediate onset times. In these configurations, relatively high-permeability layers positioned near the top enhanced vertical connectivity, thereby facilitating the earlier destabilization of the diffusive boundary layer. Notably, the stochastic formation triggered convection most rapidly, with an onset time of only 8.87 years. This behavior suggests that random heterogeneity enhances local permeability contrasts and promotes the development of preferential flow paths, which in turn accelerates the growth of convective instabilities.

Overall, these results highlight that during CO_2 geological sequestration, the stratigraphic architecture exerts a first-order control on the timing of convective onset. In particular, formations with high-permeability zones near the top or with strong small-scale heterogeneity are more prone to the early onset of density-driven convection, whereas formations with low-permeability barriers near the top can significantly delay convective initiation.

3.2 CO_2 migration

In order to analyze the migration of CO_2 in the strata, the distribution of dissolved CO_2 under different stratigraphic conditions was plotted (Figs. 2-8). In the homogeneous model (Fig. 2), convection initiates relatively early, producing dense and vertically elongated plumes that penetrated deeply into the domain within a few hundred years. This configuration promotes efficient vertical transport and rapid mixing of dissolved CO_2 throughout the formation.

In the randomly layered model (Fig. 3), the finger-like plumes are less continuous and exhibit frequent lateral deflections, indicating that the stratified heterogeneity disrupts vertical connectivity and causes plume diversion along high-permeability layers. Nevertheless, convective instability develops within a few hundred years and eventually spreads throughout the domain.

In the stochastic model (Fig. 4), convective plumes emerge very early and propagate rapidly, forming broad preferential flow channels that reach the bottom boundary within several hundred years. The high degree of small-scale heterogeneity appears to enhance local density contrasts and accelerates the onset and growth of convection, resulting in the fastest vertical CO_2 migration among all cases.

In contrast, the positive rhythmic model (Fig. 5) shows a markedly delayed onset and slower plume development. The gradual upward increase in permeability restricts downward migration, forcing the plumes to remain shallow for prolonged periods (>600 years) before deeper penetration occurs. Conversely, the reverse rhythmic model (Fig. 6) allows early plume initiation and relatively rapid propagation because high-permeability layers near the top facilitate downward flow.

The coarse-first model (Fig. 7) displays shallow but laterally extensive plumes at early stages, with CO_2 moving horizontally within the top high-permeability layers before gradually descending. This lateral spreading reduces the vertical density gradient and delayed the formation of strong vertical fingers. In contrast, the fine-first model (Fig. 8) exhibits the slowest and weakest plume development. The low-permeability layers at the top form a strong barrier to vertical mass transfer, significantly suppressing convective instabilities and confining dissolved CO_2 to the upper part of the formation even after several thousand years.

To complement the qualitative plume-morphology analysis, the evolution of sweep efficiency was also quantified for all stratigraphic architectures (Fig. 9). Sweep efficiency was defined as the volume fraction of the domain in which the dissolved CO_2 mass fraction exceeds 0.015. Fig. 9 presents the evolution of sweep efficiency for all seven stratigraphic architectures over both the early period (0-1,600 years) and the full simulation time (0-10,000 years). The quantitative results confirm the qualitative plume behaviors described in Section 3.2. Architectures characterized by early, vertically continuous fingering (stochastic and reverse rhythmic) exhibit the most rapid increase in sweep efficiency and reach full-domain sweep within approximately 2,000-2,500 years. In contrast, models with low-permeability caps (positive rhythmic, fine-first) show slow and nearly linear sweep efficiency growth, consistent with their shallow, laterally constrained plumes. The coarse-first architecture displays early lateral spreading and delayed vertical penetration, resulting in a distinct two-stage sweep-efficiency curve. The homogeneous and randomly layered cases fall between these end-members and largely validate the trends identified from the plume snapshots.

Overall, these results demonstrate that stratigraphic architecture exerts a dominant control on CO_2 migration patterns after the onset of density-driven convection. High-permeability zones near the top (reverse rhythmic, stochastic) accelerate vertical finger development, whereas low-permeability barriers (positive rhythmic, fine-first) suppress or delay vertical convection and promote lateral spreading. These contrasting behaviors directly affect the spatial distribution, dissolution rate and long-term sequestration security of injected CO_2.

3.3 CO_2 phase transformation

In order to quantify the conversion from supercritical to dissolved CO_2, we analyzed the time evolution of the dissolved-to-total CO_2 mass ratio (Figs. 10-11). Two kinetic metrics were adopted: t_{50} (time to reach a dissolved fraction

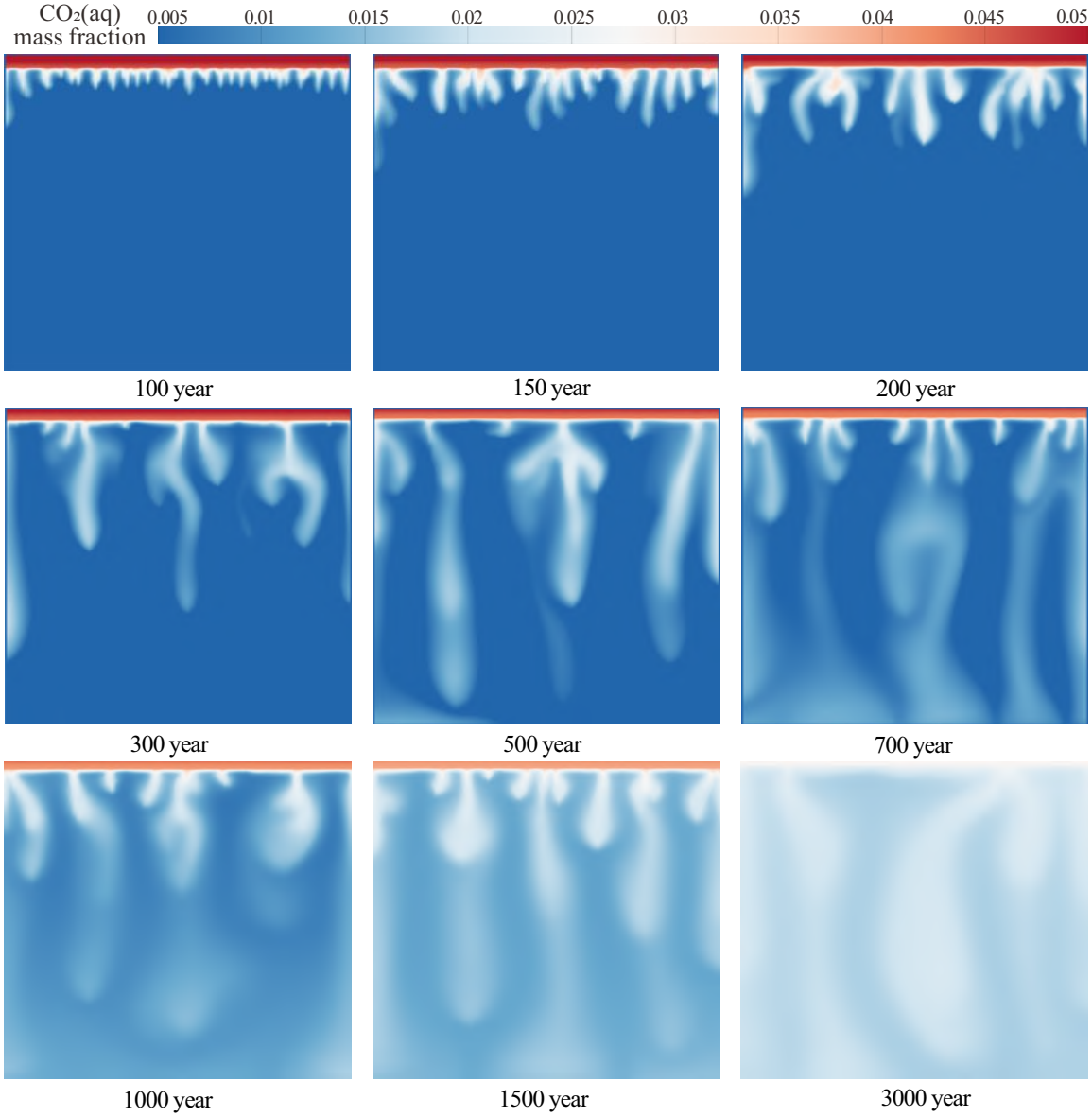

Fig. 2. Temporal evolution of dissolved CO_2 mass fraction in the homogeneous formation at different times.

of 0.5) and t_{90} (time to reach 0.9). These metrics compactly summarize the dissolution kinetics across stratigraphic architectures and complement the plume morphologies in Figs. 2-8.

3.3.1 Fast-conversion systems

Both the stochastic and reverse rhythmic formations exhibited the fastest conversion, achieving $t_{50} \approx 0.8\text{-}1.0 \times 10^3$ years and $t_{90} \approx 2.2\text{-}2.6 \times 10^3$ years (Figs. 10(b) and 11(b)). Early and deep finger penetration, favored by high connectivity in the upper reservoir and small-scale heterogeneity, shortens the diffusive stage and quickly establishes convection-dominated mixing (Figs. 4 and 6).

3.3.2 Moderate-conversion systems

The homogeneous case provides a benchmark with $t_{50} \approx 0.9\text{-}1.0 \times 10^3$ years and $t_{90} \approx 2.8\text{-}3.2 \times 10^3$ years (Fig. 9). The randomly layered sequence is slightly slower, with $t_{50} \approx 1.0\text{-}1.1 \times 10^3$ years and $t_{90} \approx 3.0\text{-}3.5 \times 10^3$ years, because plume paths are intermittently deflected along layered contrasts (Figs. 3 and 10(a)).

The randomly layered formation exhibits plume behaviors that closely resemble the homogeneous case. This occurs because the permeability values in the randomly layered model fluctuate only slightly around the mean (75 mD), with relatively small deviations in both the maximum and minimum values. Such limited contrasts do not generate strong barriers or preferential high-permeability pathways. Furthermore, the thin layers are uncorrelated in the vertical direction, preventing the development of persistent sequences of high or low permeability. At the scale of the convective fingers, these modest and randomly distributed variations become effectively averaged, producing an emergent permeability field that behaves similarly to a homogeneous medium. As a result, the descent rate, plume geometry, and sweep-efficiency evolution

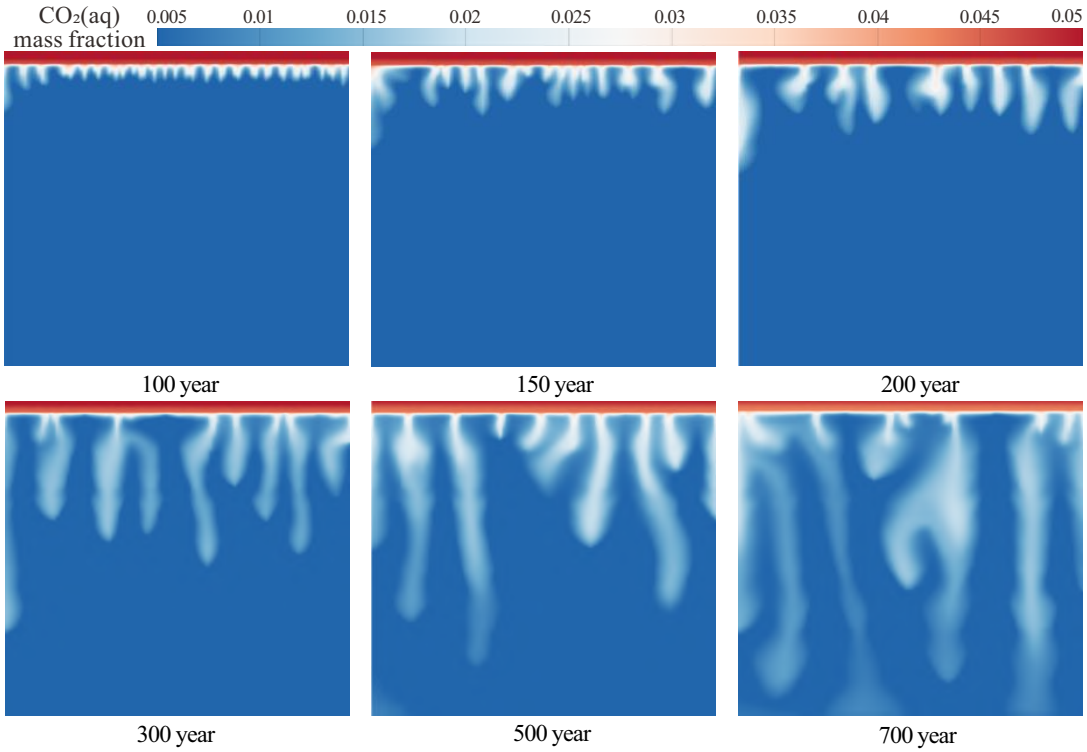

Fig. 3. Temporal evolution of dissolved CO_2 mass fraction in the randomly layered formation at different times.

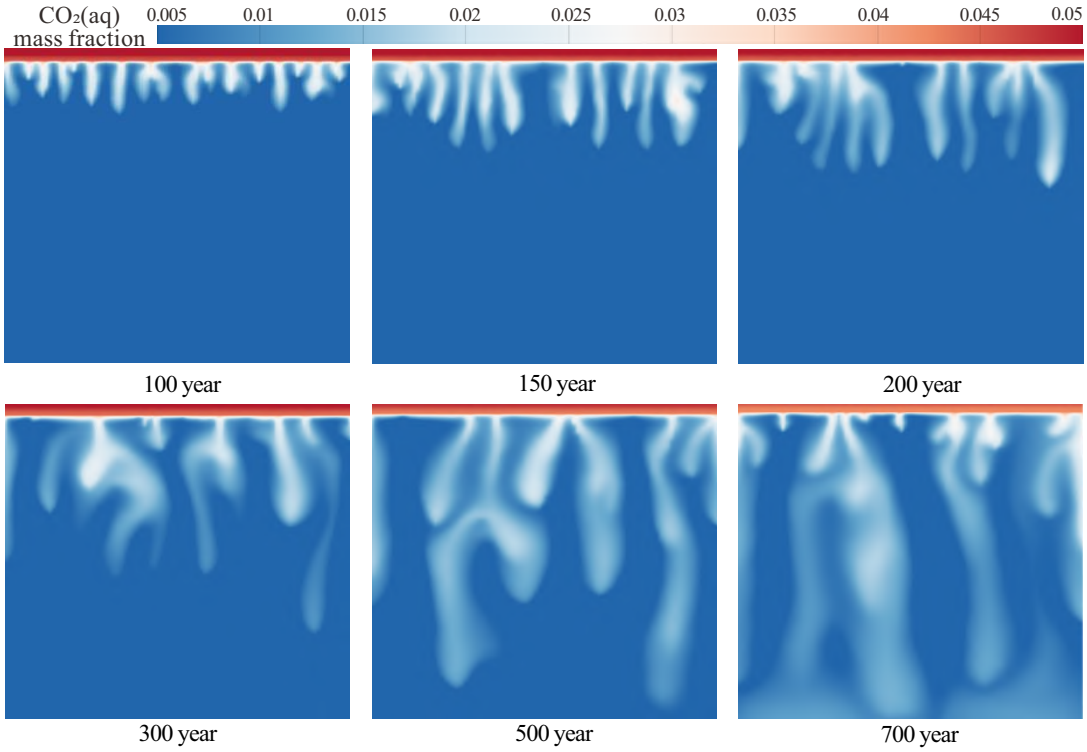

Fig. 4. Temporal evolution of dissolved CO_2 mass fraction in the stochastic formation (normally distributed porosity-permeability) at different times.

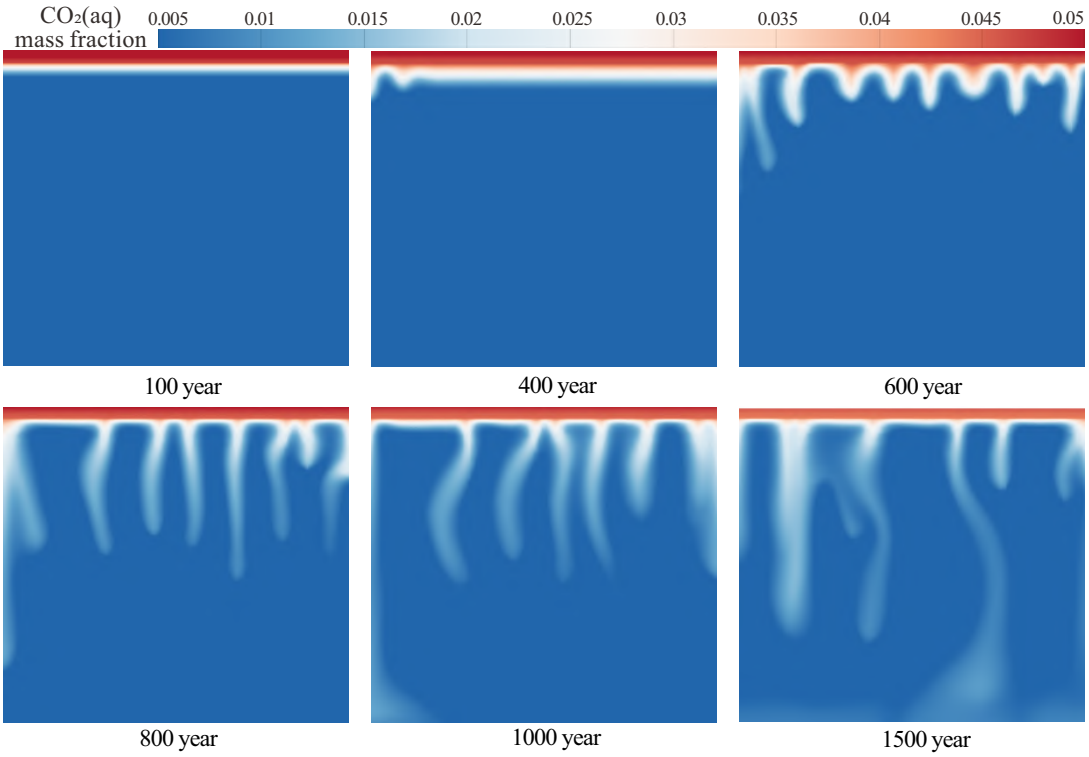

Fig. 5. Temporal evolution of dissolved CO_2 mass fraction in the positive rhythmic formation at different times.

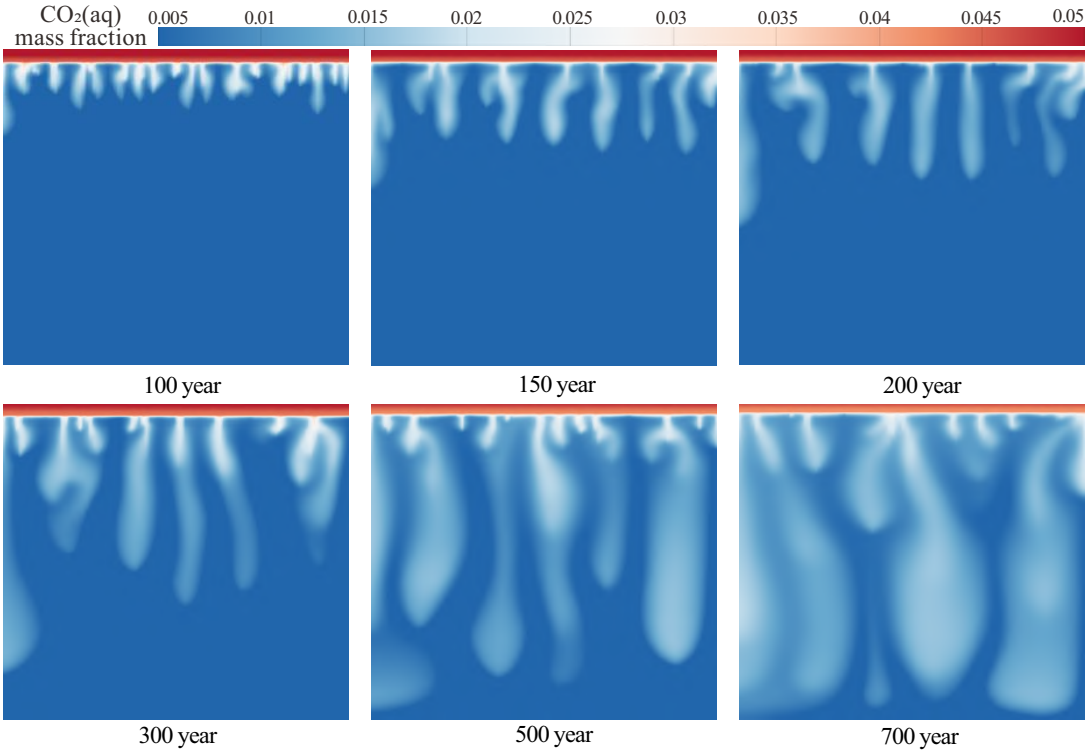

Fig. 6. Temporal evolution of dissolved CO_2 mass fraction in the reverse rhythmic formation at different times.

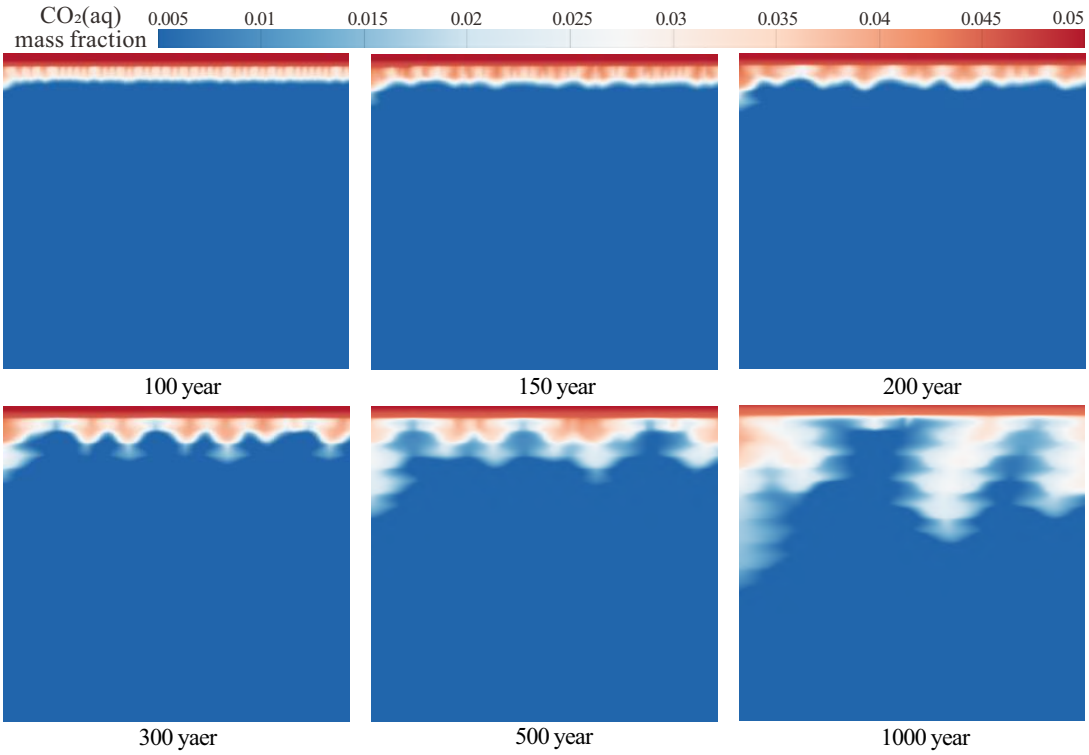

Fig. 7. Temporal evolution of dissolved CO_2 mass fraction in the coarse-first alternating formation at different times.

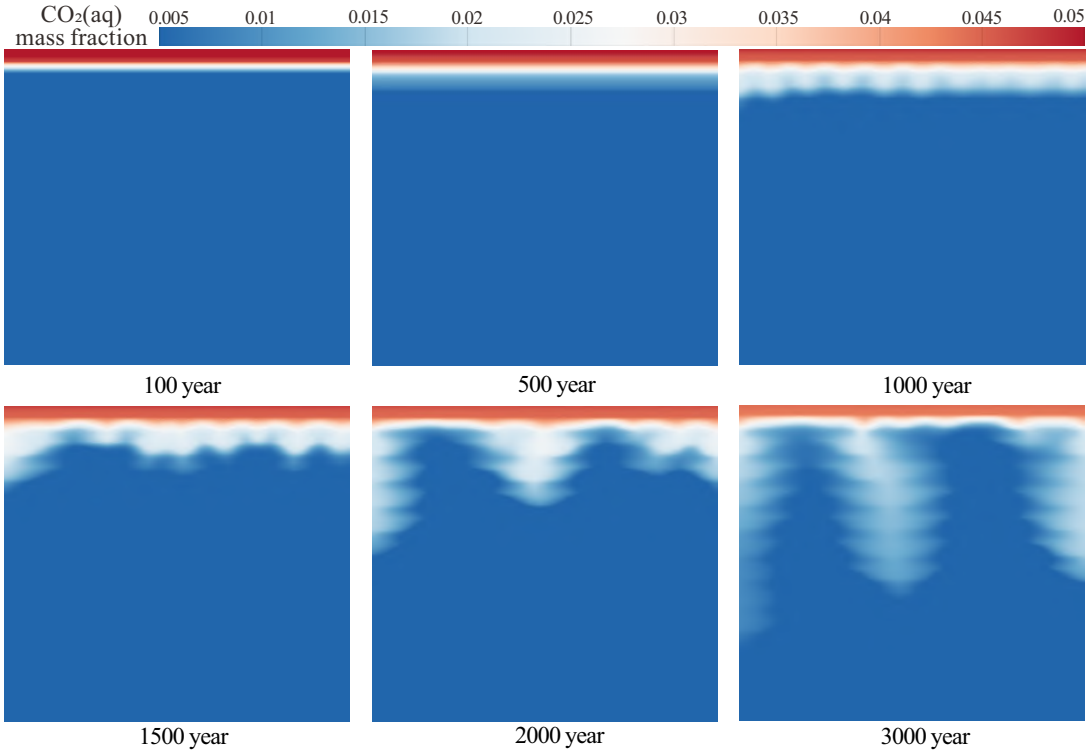

Fig. 8. Temporal evolution of dissolved CO_2 mass fraction in the fine-first alternating formation at different times.

Table 3. Kinetic metrics of CO_2 dissolution across stratigraphic architectures.

Case	Early slope	t_{50} ($\times 10^3$ years)	t_{90} ($\times 10^3$ years)	Key features/Mechanisms
Homogeneous	0.60	0.9-1.0	2.8-3.2	Dense, vertically elongated plumes; fast vertical connectivity; high mixing efficiency.
Randomly layered	0.55	1.0-1.1	3.0-3.5	Layered deflection; moderate delay vs. homogeneous; eventual domain-wide spread.
Stochastic	0.68	0.8-0.9	2.2-2.5	Small-scale heterogeneity enhances local contrasts; earliest onset and fastest propagation.
Reverse rhythmic	0.70	0.8-1.0	2.2-2.6	High-permeability layers near top facilitate early plume initiation and rapid descent.
Positive rhythmic	0.30	2.3-2.7	8.0-9.0	Low-permeability top barrier; prolonged shallow retention; delayed convection.
Coarse-first	0.25	3.0	7.0-7.5	Strong early lateral spreading within top high-permeability layer, weaker vertical descent.
Fine-first	0.18	5.0-6.0	11.0-12.0	Top low-permeability barrier; shortest fingers; slowest overall progression.

Notes: The kinetic metrics reported in this table (Early slope, t_{50}, and t_{90}) represent approximate values.

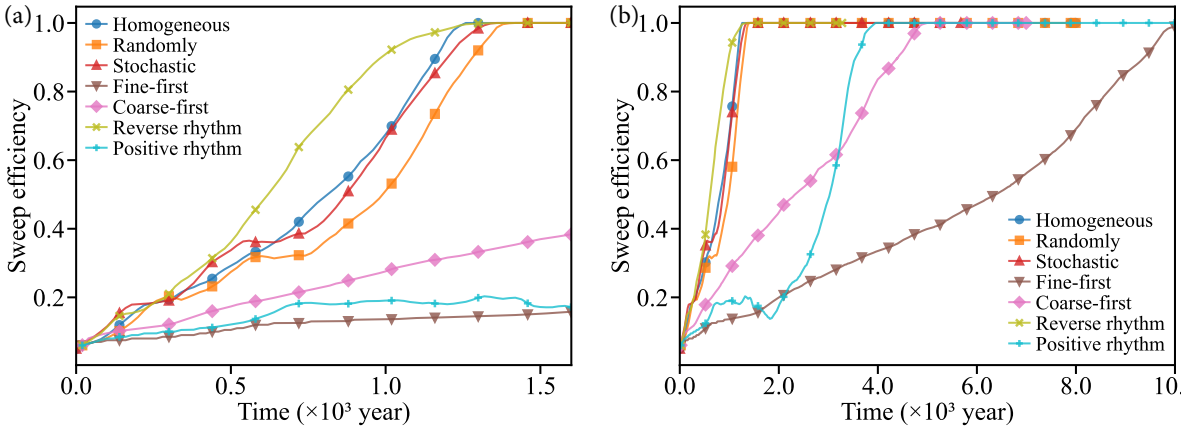

Fig. 9. Evolution of sweep efficiency for the seven stratigraphic architectures over (a) 0-1,600 years and (b) 0-10,000 years.

of the randomly layered case align much more closely with the homogeneous model than with the layered architectures that contain systematic vertical trends.

3.3.3 Slow-conversion systems

When low-permeability material occupies the upper layers, dissolution is markedly delayed. The positive rhythmic case yields $t_{50} \approx 2.3\text{-}2.7 \times 10^3$ years and $t_{90} \approx 8\text{-}9 \times 10^3$ years (Fig. 11(a)), consistent with shallow, long-lived plumes (Fig. 5). In the coarse-first architecture, despite early onset, CO_2 spreads laterally within the high-permeability cap before descending, giving $t_{50} \approx 3.0 \times 10^3$ years and $t_{90} \approx 7.0\text{-}7.5 \times 10^3$ years (Figs. 7 and 11(c)). The fine-first configuration is slowest, with $t_{50} \approx 5\text{-}6 \times 10^3$ years and $t_{90} \approx 11\text{-}12 \times 10^3$ years (Fig. 11(d)), as the low-permeability top barrier thins the CO_2-enriched boundary layer and inhibits finger amplification (Fig. 8).

Across all cases (Table 3), the ordering of dissolution kinetics is: Stochastic $\approx$ Reverse rhythmic $>$ Homogeneous $>$ Randomly layered $\gg$ Positive rhythmic $>$ Coarse-first $\gg$ Fine-first. This mirrors the onset times in Section 3.1: Earlier convective onset generally correlates with shorter t_{50} and t_{90}. Deviations (e.g., coarse-first) occur when early onset is accompanied by pronounced lateral channeling that weakens vertical density gradients. Overall, permeability distribution near the top boundary and the scale of heterogeneity jointly control both the timing and the efficiency of convective dissolution. Architectures with high-permeability pathways at shallow depth (reverse rhythmic, stochastic) accelerate solubility trapping, whereas low-permeability caps (positive rhythmic, fine-first) prolong the dissolution timescale and favor lateral spreading, implying longer monitoring horizons or targeted operational strategies to enhance mixing.

3.4 Grid-independence verification

A mesh-convergence test was performed to ensure that the 100×200 grid (20,000 cells) used in this study provides adequate spatial resolution for capturing density-driven con-

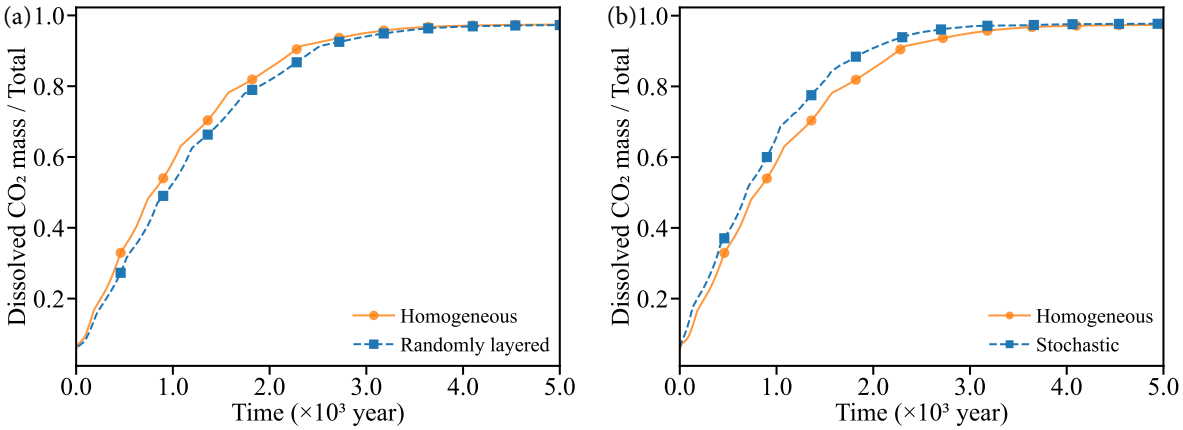

Fig. 10. Temporal evolution of the ratio of dissolved CO_2 mass to total CO_2 mass under different stratigraphic conditions: (a) Homogeneous vs. randomly layered formations and (b) homogeneous vs. stochastic formations.

vection. Additional simulations were carried out using 5,000-10,000-cell coarse grids and 30,000-40,000-cell refined grids. The variation of the completion time of CO_2 dissolution with respect to grid resolution for three representative stratigraphic architectures, homogeneous, layered, and stochastic, is generated by small-scale heterogeneity (stochastic in Fig. 12). The results indicate that solution sensitivity decreases substantially once the grid exceeds approximately 15,000 cells. The adopted 20,000-cell grid lies within the converged region, and further refinement leads to changes of less than 3-5% in key metrics such as convective onset time, plume morphology, and kinetic parameters (t_{50} and t_{90}). This confirms that the baseline grid used in the simulations is sufficiently fine to resolve the dominant convective features.

Therefore, the adopted 100×200 (20,000-cell) grid provides a sufficient balance between numerical accuracy and computational efficiency while capturing all essential convective structures. The manuscript has been updated accordingly to include these new results and a brief discussion of grid convergence.

4. Limitations and future work

Although this study provides a systematic comparison of seven stratigraphic architectures, it relies on two-dimensional (2D) numerical models that inevitably simplify the three-dimensional (3D) nature of real sedimentary basins. The 2D framework is widely used in fundamental studies of density-driven convection because it captures the primary instability mechanisms, the onset of gravitational fingering, and the essential dissolution kinetics at a substantially reduced computational cost. This dimensional reduction enables comprehensive parameter exploration and consistent comparison across heterogeneous architectures.

Nevertheless, 3D systems can exhibit additional complexities, including enhanced finger branching, asymmetric plume spreading, and more intricate lateral connectivity. These features generally promote faster perturbation growth, earlier convection onset, and slightly higher dissolution efficiencies compared with 2D systems. Such differences may shift the absolute values of onset or completion time, particularly in formations with strong anisotropy or channelized heterogeneity. However, they do not alter the underlying physical mechanisms identified in this study. The relative influence of permeability architecture, vertical connectivity, and shallow-layer contrasts, as well as the resulting hierarchy of convective behavior, are primarily controlled by permeability distributions near the upper boundary and are expected to remain consistent in 3D settings. Future work will extend the present analysis to fully 3D simulations incorporating multiscale heterogeneity, reactive transport and potential geomechanical coupling, to further quantify the magnitude of 3D effects and evaluate the robustness and generality of the conclusions.

In addition, the conceptual models in this study adopt uniform 4-m layer thickness and zero-flux boundaries to isolate the role of permeability architecture on convective mixing. This idealization follows standard practice in mechanistic convection studies and ensures that variations in convective onset and dissolution kinetics arise solely from differences in permeability distribution rather than geometric variability or external flow. In real reservoirs, however, layer thickness may vary significantly and boundaries may be hydrodynamically open. While such features can influence the magnitude of mixing or the lateral extent of plume spreading, the primary mechanisms identified here, the control of vertical connectivity and shallow permeability on early convective instability, remain applicable. Variable-thickness sequences effectively modify the relative contribution of high- and low-permeability intervals, but they do not change the mechanistic hierarchy observed across the seven stratigraphic architectures. Future work will incorporate realistic stratigraphic geometries, open-boundary conditions, and field-scale reservoir architectures to further evaluate the transferability of the results to natural geological settings.

5. Conclusions

This study investigates how stratigraphic architecture controls the onset, morphology, and long-term efficiency of density-driven dissolution during geological CO_2 sequestration. Using TOUGH2-ECO2N and seven conceptual forma-

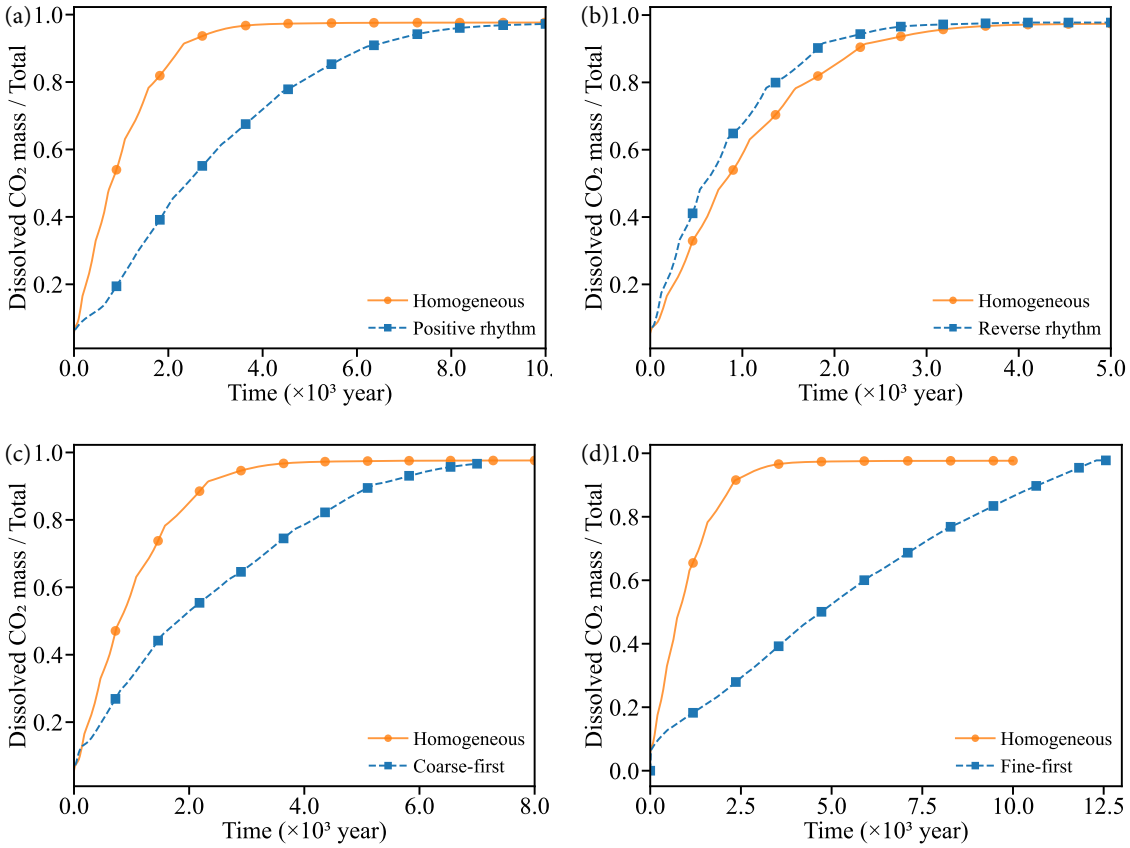

Fig. 11. Temporal evolution of the ratio of dissolved CO_2 mass to total CO_2 mass under different stratigraphic conditions: (a) Homogeneous vs. positive rhythmic, (b) homogeneous vs. reverse rhythmic, (c) homogeneous vs. coarse-first, and (d) homogeneous vs. fine-first formations.

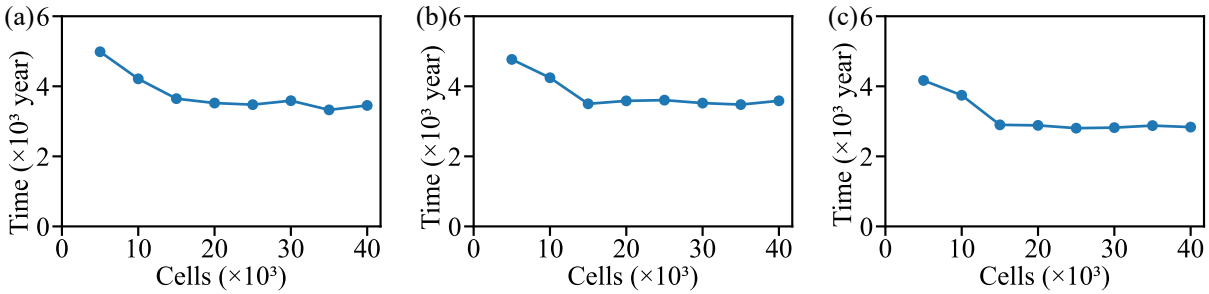

Fig. 12. Mesh convergence results showing the completion time of CO_2 dissolution under different grid resolutions (5,000-40,000 cells) for (a) homogeneous, (b) randomly layered, and (c) stochastic formations.

tions, homogeneous, randomly layered, stochastic (normally distributed), positive rhythmic, reverse rhythmic, coarse-first, and fine-first, this work simulated the transition of a top supercritical CO_2 layer into the dissolved phase and quantified system-scale kinetics by the dissolved/total CO_2 mass ratio. The main conclusions obtained are as follows:

1) Stratigraphy exerts first-order control on convective onset. Onset times span nearly two orders of magnitude, from 8.87 years (stochastic) to 885.34 years (fine-first). High-permeability pathways near the top, either imposed systematically (reverse rhythmic, 23.56 years) or created by small-scale heterogeneity (stochastic), trigger the earliest instabilities. Low-permeability caps (positive rhythmic, 338.91 years; fine-first) delay convection substantially, while the homogeneous (35.22 years) and randomly layered (43.36 years) cases lie in between.
2) Dissolution kinetics follow a consistent hierarchy across formations. From the time histories of dissolved CO_2 fraction (Figs. 10-11), the characteristic times to reach 50% and 90% dissolution are ordered as Stochastic $\approx$ Reverse rhythmic $>$ Homogeneous $>$ Randomly layered $\gg$ Positive rhythmic $>$ Coarse-first $\gg$ Fine-first. This

hierarchy mirrors onset times, confirming a strong linkage between early instability and system-scale conversion.

3) Migration patterns diagnose the kinetic outcomes. Plume morphologies (Figs. 2-8) explain the kinetic contrasts: Rapid, vertically continuous fingers in stochastic and reverse rhythmic formations accelerate mixing; layered deflection in randomly layered media causes only a modest slowdown; positive rhythmic and fine-first architectures impose shallow, long-lived CO_2-enriched layers that inhibit vertical flux. Coarse-first is a mechanistic outlier, despite early onset, high-permeability lenses at the top drive pronounced lateral spreading, weakening vertical density gradients and delaying t_{90}.
4) Implications for sequestration design and monitoring. Formations with high-permeability pathways near the top (reverse rhythmic, stochastic) promote early solubility trapping, shortening the period with mobile supercritical CO_2 and potentially reducing monitoring burdens. In contrast, low-permeability caps (positive rhythmic, fine-first) prolong dissolution timescales and favor lateral dispersion, implying longer monitoring horizons and motivating operational strategies (e.g., well placement, engineered mixing) to enhance vertical exchange.
5) Dominance of Stratigraphy-Controlled Convection Over Early Onset. While the onset of convection provides a useful indicator of the initial instability, the ultimate dissolution efficiency is controlled by the long-term convective regime that develops afterward. This regime, characterized by finger persistence, vertical connectivity and the degree of lateral channeling, is fundamentally dictated by the stratigraphic architecture. Thus, early onset alone does not determine the overall effectiveness of CO_2 dissolution; rather, it is the stratigraphy-controlled convective evolution that governs the final mixing performance.

Overall, the distribution of permeability in the upper reservoir and the scale of heterogeneity jointly govern both the timing (onset) and efficiency (t_{50}, t_{90}) of convective dissolution. Recognizing and leveraging these stratigraphic controls is essential for reliable performance assessment and risk-informed design of geological CO_2 sequestration.

Acknowledgements

This work was supported by the National Natural Science Foundation of China (No. U2244215), and supported by Graduate Innovation Fund of Jilin University, the Key Laboratory of Groundwater Resources and Environment, Ministry of Education, Jilin University, and by the Jilin Provincial Key Laboratory of Water Resources and Water Environment, Jilin University.

Conflict of interest

The authors declare no competing interest.

References

Ajayi, T., Gupta, I. A review of reactive transport modeling in wellbore integrity problems. Journal of Petroleum Science and Engineering, 2019, 175: 785-803.

Amarasinghe, W. S., Fjelde, I., Flaata, A. M. N. Visual investigation of CO_2 dissolution and convection in heterogeneous porous media at reservoir temperature and pressure conditions. Greenhouse Gases: Science and Technology, 2021, 11(2): 342-359.

Awag, M., Mackay, E., Ghanbari, S. Impact of CO_2 solubility on design of single well tracer tests to evaluate residual saturation during carbon capture and storage. Advances in Geo-Energy Research, 2024a, 11(1): 6-19.

Awag, M., Mackay, E., Ghanbari, S. A numerical analysis of background flow velocity effects on long-term post-injection migration of CO_2 plumes in tilted storage aquifers. Advances in Geo-Energy Research, 2024b, 11(2): 103-114.

Bachu, S. CO_2 storage in geological media: Role, means, status and barriers to deployment. Progress in Energy and Combustion Science, 2008, 34(2): 254-273.

Benson, S. M., Cole, D. R. CO_2 sequestration in deep sedimentary formations. Elements, 2008, 4(5): 325-331.

Brouzet, C., Méheust, Y., Meunier, P. CO_2 convective dissolution in a three-dimensional granular porous medium: An experimental study. Physical Review Fluids, 2022, 7: 033802.

Corey, A. T. The interrelation between gas and oil relative permeabilities. Producers Monthly, 1954, 19: 38-41.

De Paoli, M., Zonta, F., Soldati, A. Influence of anisotropic permeability on convection in porous media: Implications for geological CO_2 sequestration. Physics of Fluids, 2016, 28(5): 056601.

Emami-Meybodi, H., Hassanzadeh, H., Green, C. P., et al. Convective dissolution of CO_2 in saline aquifers: Progress in modeling and experiments. International Journal of Greenhouse Gas Control, 2015, 40: 238-266.

Faramarzi, M., Tabatabaei, S. M., Sedaee, B., et al. Saturation-functions models in CO_2-brine system: A comparative study. Capillarity, 2025, 14(2): 35-52.

Fruton, P., Nauruzbaeva, A., Bataller, H., et al. Convective dissolution of carbon dioxide into brine in a three-dimensional free medium. Physical Review Fluids, 2023, 8(2): 023503.

Guo, R., Sun, H., Zhao, Q., et al. A novel experimental study on density-driven instability and convective dissolution in porous media. Geophysical Research Letters, 2021, 48(23): e2021GL095619.

Hesse, M. A., Orr, F. M., Tchelepi, H. A. Gravity currents with residual trapping. Journal of Fluid Mechanics, 2008, 611: 35-60.

Hidalgo, J. J., Carrera, J. Effect of dispersion on the onset of convection during CO_2 sequestration. Journal of Fluid Mechanics, 2009, 640: 441-452.

Hidalgo, J. J., Fe, J., Cueto-Felgueroso, L., et al. Scaling of convective mixing in porous media. Physical Review Letters, 2012, 109(26): 264503.

Hu, C., Xu, K., Yang, Y. Effects of the geothermal gradient on the convective dissolution in CO_2 sequestration. Journal of Fluid Mechanics, 2023, 963: A23.

Jing, J., Yang, Y., Tang, Z. Assessing the influence of injection temperature on CO_2 storage efficiency and capacity in the sloping formation with fault. Energy, 2021, 215: 119097.

Jing, J., Yang, Y., Cheng, J., et al. CO_2 injection capacity assessment by considering layered heterogeneity: A case study in a shenhua-ccs reservoir, China. Journal of Hydrology, 2025, 650: 132547.

Juanes, R., Spiteri, E. J., Orr, F. M., et al. Impact of relative permeability hysteresis on geological CO_2 storage. Water Resources Research, 2006, 42(12): W12418.

Li, B., Benson, S. M. Influence of small-scale heterogeneity on upward CO_2 plume migration in storage aquifers. Advances in Water Resources, 2015, 83: 389-404.

Li, D., Chen, Y., Chen, S. Convective dissolution in layered porous media with application to CO_2 geological sequestration: Experimental and numerical insights into layering configuration and interface angle. Journal of Hydrology, 2025, 662: 133952.

Liu, H., Chen, J., Jin, G., et al. Determination of CO_2 convective mixing flux in saline aquifers based on the optimality. Advances in Geo-Energy Research, 2024, 13(2): 89-95.

Li, Y., Yang, Y., Dong, M. CO_2 capillary trapping in layered sandstone dominated by inertial force and gravity. Capillarity, 2024, 10(1): 22-28.

Luther, E. E., Dallaston, M. C., Shariatipour, S. M., et al. Onset of convective instability in an inclined porous medium. Physics of Fluids, 2022, 34(1): 014104.

MacMinn, C. W., Juanes, R. Buoyant currents arrested by convective dissolution. Geophysical Research Letters, 2013, 40(10): 2017-2022.

Mahyapour, R., Mahmoodpour, S., Singh, M., et al. Effect of permeability heterogeneity on the dissolution process during carbon dioxide sequestration in saline aquifers: Two-and three-dimensional structures. Geomechanics and Geophysics for Geo-Energy and Geo-Resources, 2022, 8: 70.

Michael, K., Golab, A., Shulakova, V., et al. Geological storage of CO_2 in saline aquifers-a review of the experience from existing storage operations. International Journal of Greenhouse Gas Control, 2010, 4(4): 659-667.

Neufeld, J. A., Hesse, M. A., Riaz, A., et al. Convective dissolution of carbon dioxide in saline aquifers. Geophysical Research Letters, 2010, 37(22): L22404.

Pau, G. S. H., Bell, J. B., Pruess, K., et al. High-resolution simulation and characterization of density-driven flow in CO_2 storage in saline aquifers. Advances in Water Resources, 2010, 33(4): 443-455.

Pruess, K. The TOUGH codes – A family of simulation tools for multiphase flow and transport processes in permeable media. Vadose Zone Journal, 2004, 3(3): 738-746.

Pruess, K., Spycher, N. ECO2N – A fluid property module for the TOUGH2 code for studies of CO_2 storage in saline aquifers. Energy Conversion and Management, 2007, 48(6): 1761-1767.

Riaz, A., Hesse, M., Tchelepi, H. A., et al. Onset of convection in a gravitationally unstable diffusive boundary layer in porous media. Journal of Fluid Mechanics, 2006, 548: 87-111.

Sayakov, O., Zhao, M. Y., Nguyen, M., et al. Revealing soil mechanics via coupled discrete and finite element method triaxial testing. Engineered Science, 2025, 36: 1648.

Sayers, J., Daniel, R. F., Hillis, R. R., et al. Carbon dioxide storage leads of the eastern gippsland basin, australia; terminology, seal and structure considerations in trap integrity assessments. Energy Procedia, 2011, 4: 4680-4687.

Shahriar, M. F., Khanal, A. Effect of formation heterogeneity on CO_2 dissolution in subsurface porous media. ACS Earth and Space Chemistry, 2023, 7: 2073-2090.

Slim, A. C. Solutal-convection regimes in a two-dimensional porous medium. Journal of Fluid Mechanics, 2014, 741: 461-491.

Soboleva, E. Instability problems and density-driven convection in saturated porous media linking to hydrogeology: A review. Fluids, 2023, 8(2): 36.

Szulczewski, M. L., MacMinn, C. W., Herzog, H. J., et al. Lifetime of carbon capture and storage as a climate-change mitigation technology. Proceedings of the National Academy of Sciences of the United States of the America, 2012, 109(14): 5185-5189.

Umirova, G., Kuttybayev, A., Khomenko, V., et al. Advanced approaches to depth optimization in large-diameter water well drilling in mangystau peninsula. Engineered Science, 2025, 36: 1605.

van Genuchten, M. T. A closed-form equation for predicting the hydraulic conductivity of unsaturated soils. Soil Science Society of America Journal, 1980, 44: 892-898.

Wang, S., Cheng, Z., Zhang, Y., et al. Unstable density-driven convection of CO_2 in homogeneous and heterogeneous porous media with implications for deep saline aquifers. Water Resources Research, 2021, 57: e2020WR028132.

Wang, Y., Chu, H., Lyu, X. Deep learning in CO_2 geological utilization and storage: Recent advances and perspectives. Advances in Geo-Energy Research, 2024, 13(3): 161-165.

Wang, Y., Fernàndez-Garcia, D., Saaltink, M. W. Carbon dioxide (CO_2) dissolution efficiency during geological carbon sequestration (GCS) in randomly stratified formations. Water Resources Research, 2022, 58: e2022WR032325.

Wang, Y., Wang, F., Wang, D., et al. Impact of through-layer fracturing on CO_2 storage efficacy of interbedded reservoirs in inclined formations. Geoenergy Science and Engineering, 2025, 255: 214132.

Xue, R., Chang, Y., Wang, S., et al. Pore-scale microfluidic investigation of unsaturated CO_2 bubble morphology and interface evolution during drainage-imbibition cycles. Capillarity, 2025, 15(3): 74-86.

Zhang, Q., Xu, Q., Yang, Y., et al. Permeability heterogeneity effects on density-driven CO_2 natural convection and carbon sequestration efficiency. Fuel, 2024, 363: 130871.